Time-dependent optical response of three-dimensional Au nanoparticle arrays formed on silica nanowires

Lorenzo Di Mario,[1] Tadele Orbula Otomalo,[2] Daniele Catone,[3] Patrick O'Keeffe,[4] Lin Tian (田琳),[1] Stefano Turchini,[3]
Bruno Palpant,[2,*] and Faustino Martelli[1,†]
[1]*Istituto per la Microelettronica e i Microsistemi (IMM), CNR, Via del Fosso del Cavaliere 100, 00133 Rome, Italy*
[2]*Laboratoire de Photonique Quantique et Moléculaire,CentraleSupélec, Ecole Normale Supérieure Paris-Saclay, Université Paris Saclay, CNRS UMR 8537, 3 rue Joliot Curie, F-91190 Gif-sur-Yvette, France*
[3]*Istituto di Struttura della Materia (ISM), CNR, Division of Ultrafast Processes in Materials (FLASHit), Via del Fosso del Cavaliere 100, 00133 Rome, Italy*
[4]*Istituto di Struttura della Materia (ISM) CNR, Division of Ultrafast Processes in Materials (FLASHit), 00016 Monterotondo Scalo, Italy*

(Received 11 October 2017; revised manuscript received 12 March 2018; published 28 March 2018)

We present stationary and transient absorption measurements on 3D Au nanoparticle (NP)-decorated SiO_2 nanowire arrays. The 3D NP array has been produced by the dewetting of a thin Au film deposited on silica nanowires produced by oxidation of silicon nanowires. The experimental behaviors of the spectral and temporal dynamics observed in the experiment are accurately described by a two-step, three-temperature model. Using an arbitrary set of Au NPs with different aspect ratios, we demonstrate that the width of the experimental spectra, the energy shift of their position with time, and the asymmetry between the two positive wings in the dynamical variation of absorption can all be attributed to the nonuniform shape distribution of the Au NPs in the sample.

DOI: 10.1103/PhysRevB.97.115448

I. INTRODUCTION

The optical response of metal nanoparticles (NPs) is dominated by the localized surface plasmon resonance (LSPR), a collective oscillation of the conduction electrons produced by incident photons with a characteristic energy. The plasmon resonance results in sharp peaks in the absorption spectrum, which are affected by the size, shape and composition of the NPs, by their environment, and by their coupling. This makes metal NPs of great interest for several applications, including molecular sensing [1], biomedical treatments [2], and optoelectronic devices [3]. Moreover, the study of the LSPR can be exploited to characterize the particles themselves, promoting the synthesis of NPs with peculiar morphologies and inspiring the fabrication of novel structures with unique functionalities [4,5]. The LSPR is a complex phenomenon, with dynamics that involve a sequence of several energy exchange processes, with different time scales, from a few femtoseconds to hundreds of picoseconds. Understanding the physics behind the processes and how each of them is affected by size, shape, and composition of the NPs and by their environment is essential to fully exploit the NPs in many applications. For isolated NPs dispersed in liquids or on a flat glass support, the ways the different dynamic processes depend on the shape and size of the NPs have been extensively studied [6]. Moreover, for most applications, the metal NPs have to be combined with other materials and the fabrication processes can strongly limit the control over the NP morphology.

Two-dimensional arrays of closely packed NPs [7] or three-dimensional assemblies of NPs [8] increase the NP interaction with the light thus enhancing the optical absorption and hence the potential sensitivity of devices. One-dimensional nanostructures and in particular nanowires (NWs) can be easily exploited as support structures for metal NPs. In fact, they can be synthesized in dense arrays, by carefully controlling their morphology and orientation with respect to the substrate. Studies have been reported where semiconductor nanowires have been decorated with metal NPs and exploited as a substrate for surface enhanced Raman spectroscopy [9,10].

In this work, we present the stationary and dynamic optical responses of Au-decorated silica nanowire arrays. The silica NW arrays have been fabricated via thermal oxidation of Si NWs grown on a quartz substrate. The structures fabricated are an excellent support for metal NPs because they provide a large surface area to attach the NPs, providing at the same time a macroporous framework that enables easy access to liquids or gases thus providing an efficient interaction with the environment [11]. This makes our arrays particularly suitable for plasmon-enhanced catalysis, a promising field of application for Au NP arrays [12,13]. Our arrays are also fully transparent in the visible to near-UV region of the spectrum, thus allowing transmission measurements. Additionally, the strong light trapping typical of the nanowire arrays [14] increases the light absorption from the NPs thus enhancing the sensitivity of the 3D arrays to the environment [11]. A two-step, three-temperature model, developed to reproduce and interpret the experimental results, is also presented that allows for the correlation of several features of the stationary and transient optical responses to the shape and shape distribution of the Au NPs in the arrays.

---

[*] bruno.palpant@ecp.fr
[†] faustino.martelli@cnr.it

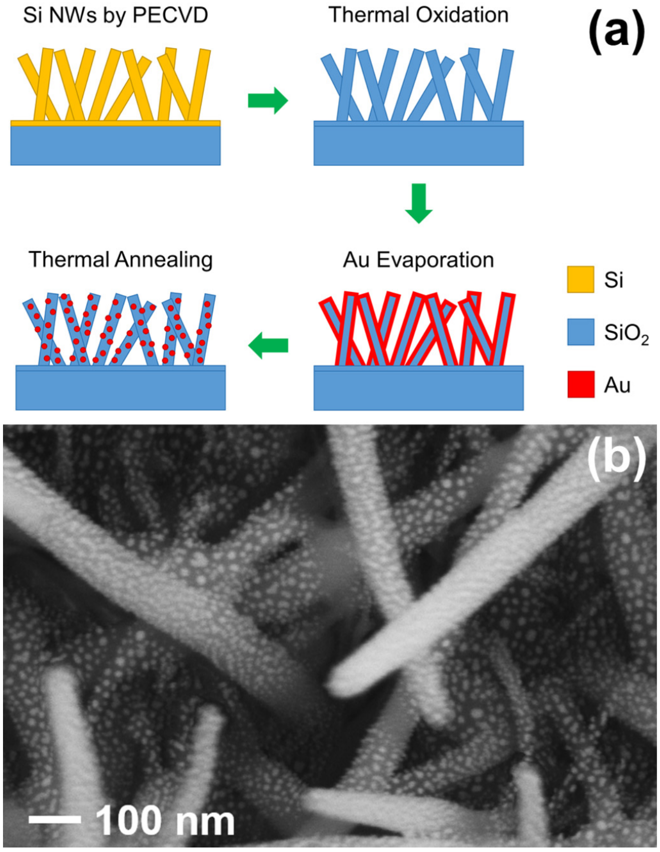

FIG. 1. (a) Schematic representation of the fabrication process of Au-decorated silica NW arrays. (b) Representative SEM image of an Au-decorated silica NW array.

II. EXPERIMENTAL

The Au-decorated SiO_2 NW arrays have been fabricated as schematically shown in Fig. 1(a). Si NWs have been grown by plasma enhanced chemical vapor deposition (PECVD) on top of a flat quartz substrate, using Au NPs as seeds in a vapor-liquid-solid (VLS) process [14]. The NW arrays have been oxidized to obtain SiO_2 NWs, and then covered with a thin layer (5 nm nominal thickness) of Au by thermal evaporation [11]. For this work, a thermal annealing at 500 °C for 1 hour has been used to obtain the Au NPs from the dewetting of the thin film. A scanning electron microscopy (SEM) image of a typical array fabricated for this work is reported in Fig. 1(b). A NW length around 2 μm has been selected in order to obtain the best compromise between a large surface area to attach the Au NPs and a good transparency of the whole structure to perform optical measurements in transmission. A dense and disordered ensemble of Au NPs has been obtained at the end of the fabrication process. An average particle size of about 15 nm in the direction parallel to the NW growth axis has been estimated by averaging over hundreds of NPs using SEM images. As for the axis perpendicular to the NW surface, the analysis of the SEM images is not a suitable way to estimate the NP size due to the difficulty in identifying the NPs with the suitable orientation for accurate measurements. On the other hand, the SEM images clearly show a low contact angle between the NPs and the NW surface suggesting that the NP shape can be well approximated by an oblate ellipsoid.

Stationary absorbance spectra of the NP arrays have been obtained measuring both transmission and reflection in the visible range with a Perkin-Elmer spectrophotometer, equipped with an integration sphere to collect all the light scattered by the SiO_2 NWs. Transient absorption (TA) spectroscopy measurements have been performed in a pump-probe experiment where the optical pump consists of the second harmonic of a Ti:Sapphire laser at 405 nm with a pulse length shorter than 50 fs and a repetition rate of 1 kHz. Under these conditions, after pump excitation, a complete dissipation of the heating induced by the pump occurs prior to the subsequent pulse. A white light supercontinuum generated in a femtosecond transient absorption spectrometer (FTAS) of IB Photonics (FemtoFrame II) has been used as the probe. The probe wavelengths ranged between 330 and 750 nm, while the pump-probe delay time lasted up to 500 ps, with an overall temporal resolution of around 50 fs. The measurements have been performed using four different pump-pulse intensities (0.4, 0.8, 2, and 4 $\mathrm{GWcm^{-2}}$).

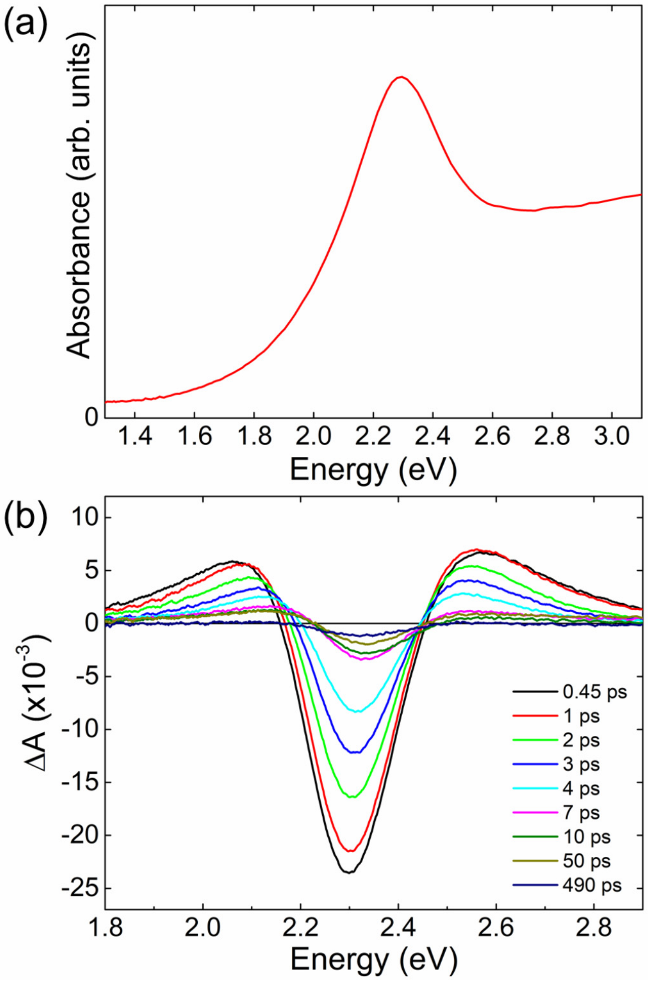

FIG. 2. (a) Experimental absorbance spectrum of the Au-decorated silica NW array. (b) Experimental spectral dependence of the transient absorption for different delay times between pump and probe pulses. ΔA is defined as the absorbance difference of the probe after and before pump excitation.

III. EXPERIMENTAL RESULTS

The absorbance of the NP/NW array in the visible range is shown in Fig. 2(a). Due to the transparency of the SiO_2 NW array in the explored energy range, the spectrum only represents the Au NP optical response, with a well-defined LSPR band peaked at 2.3 eV superimposed on a rising absorption starting from ∼2.0 eV, due to interband electronic transitions.

Using a white light supercontinuum as probe for the TA spectroscopy measurements, the variation of the absorbance (ΔA) of the sample after the pump pulse excitation depends on both the probe wavelength and the delay time between pump and probe. For the sake of clarity, the TA results are shown and discussed separating the spectral and the temporal dependence. Figure 2(b) shows the spectral dependence of the TA of the Au-decorated SiO_2 NW array, for different pump-probe delays, acquired with a pump-pulse intensity of $2\,\mathrm{GWcm}^{-2}$. Similar behaviors have been obtained for the different pump intensities. Three main features characterize the spectra: a negative minimum of the signal at the LSPR, which corresponds to the bleaching of the plasmon resonance and two positive signals at both wings of the LSPR. The main effect of the ultrafast light absorption is the increase in the electronic temperature (T_e) with the ensuing broadening of the plasmon band. This leads to a transient reduction of the absorption near the plasmon maximum and to a transient absorption increase in the wings of the band [15]. At short delays, the positive wings have different magnitudes, presenting an evident asymmetry that disappears for time delays longer than 10 ps. Furthermore, a blueshift of the bleaching of the LSPR can be observed for the first 20 ps.

The temporal dependence of the TA at different probe energies around the LSPR energy is reported in Fig. 3(a) for time delays up to 10 ps. All the probe energies show similar dynamics, which can be described by single exponential decays, indicating that a single process is dominant in this time range: the electron-phonon coupling. The dynamics becomes slower for increasing probe photon energy, as it will be discussed below. This is consistent with the observation of a blue shift of the minimum during the first picoseconds.

Fitting the time decay at 2.3 eV, corresponding to the stationary LSPR, it is possible to determine the electron-phonon coupling characteristic time from the relaxation time constant. However, data from single pump pulse intensity are not sufficient, since the relaxation time depends on the excitation intensity. The standard approach consists in performing measurements with different intensities and plotting the relaxation times obtained as a function of that intensity as shown in Fig. 3(b). The electron-phonon coupling time can then be extrapolated by performing a linear fit of the data and looking at the zero power intercept [16]. The fit gives a value of the electron-phonon coupling time constant for our Au NPs array of $\tau_{\text{e-ph}} = 0.95 \pm 0.06\,\mathrm{ps}$, in agreement with what is expected for our NP size [17].

IV. MODEL

We have used a three-temperature model (3TM) to simulate the electron $T_e(t)$ and lattice $T_l(t)$ temperature profiles of the Au NPs as well as the temperature of the surrounding medium. The model consists of coupled differential equations describing the energy exchanges between the light wave, the electron gas, the metal ionic lattice and the surrounding medium [18,19]:

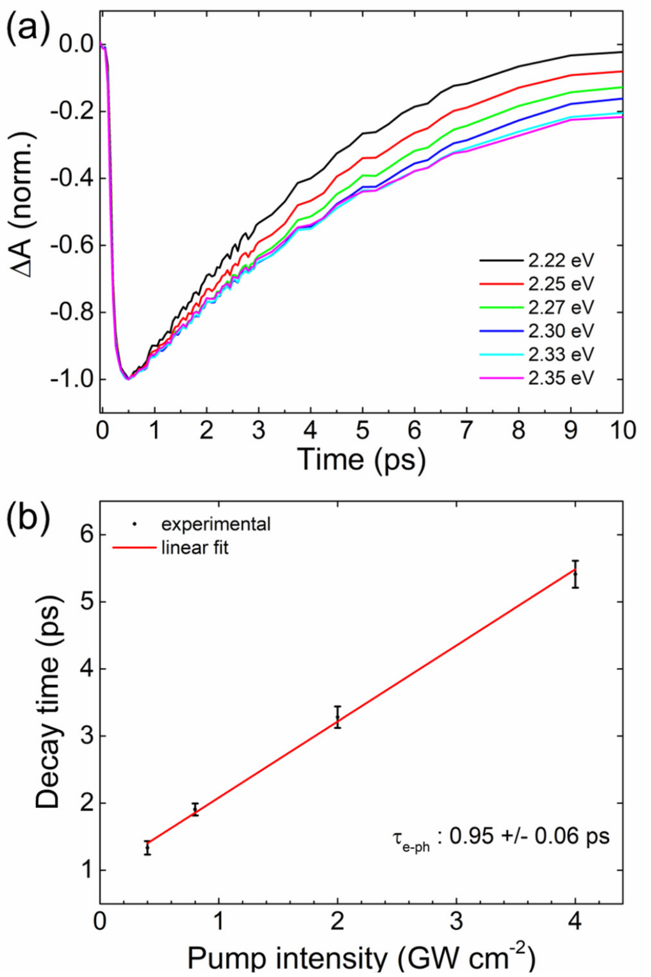

FIG. 3. (a) Experimental time dependence of ΔA at different probe energies. (b) Decay time of ΔA at the energy of the minimum as a function of the pump intensity.

$$C_e \frac{\partial T_e}{\partial t} = -G(T_e - T_l) + P_{abs}(t), \tag{1}$$

$$C_l \frac{\partial T_l}{\partial t} = G(T_e - T_l) - \frac{H(t)}{V}, \tag{2}$$

where C_e and C_l denote the electron gas and lattice specific heats, respectively. Considering quasifree electron behavior in noble metals, C_e is proportional to T_e at relatively low electron temperatures (up to ∼3000 K): $C_e = \gamma_e T_e$, γ_e being a constant value which depends on the type of metal in consideration (for bulk gold, $\gamma_e = 66\ \mathrm{J\,m^{-3}\,K^{-2}}$). At higher T_e, the value of C_e departs from this simple quasifree electron approach owing to the non-negligible influence of d-band electrons on the electron density of states of gold. As in [19], we have used the approach of Lin and Zhigilei [20] for $C_e(T_e)$. G and $P_{abs}(t)$ are the electron-phonon coupling constant and the instantaneous laser power absorbed per metal volume unit, respectively. Following Ref. [20], G also exhibits an electron temperature dependence at high T_e due to d-band electrons, which we account for in our model. $P_{abs}(t)$ is evaluated from the laser pulse characteristics and the NP absorption cross section [19,21]. In Eq. (2), V is the volume of the metal nanoparticle while $H(t)$ denotes the instantaneous heat released through the interface into the surrounding matrix. Considering a perfect interface between the nanoparticle and its surrounding matrix, the second term in the right-hand side of Eq. (2) can be expressed as

$$\frac{H(t)}{V} = \frac{S}{V}\kappa_m \frac{\partial T_m}{\partial r}\bigg|_{r=R}, \qquad (3)$$

where S and V are the particle surface and volume, respectively, κ_m and T_m are the host medium thermal conductivity and temperature, respectively. Assuming that the heat transport in the host medium is purely diffusive, the temperature T_m follows the Fourier law. Hence, D_m being the heat diffusion constant of the host medium, the heat equation writes

$$\frac{\partial T_m}{\partial t} = D_m \Delta T_m. \qquad (4)$$

Equation (4), together with Eqs. (1) and (2), make up the 3TM model. Since the geometry of the virtual Au NPs that we are considering here is nonspherical (as described later), Eq. (3), and hence Eq. (2) cannot be implemented directly. Thus the coupled differential equations of the 3TM model have been solved using a finite element method (using the optimization software COMSOL) [22]. The time-dependent temperatures obtained in this way have then been used to calculate the variation of the dielectric function of Au at each angular frequency ω due to the contributions from interband $[\Delta\tilde{\varepsilon}_{\omega}^{ib}(t)]$ and intraband $[\Delta\tilde{\varepsilon}_{\omega}^{D}(t)]$ electron transitions. To obtain the latter, the time evolution of the collision factor in the Drude model has been considered [21]. To obtain the interband contribution, the imaginary part has been calculated using Lindhard theory [22], considering a local parabolic band structure around the L point of the Brillouin zone (Rosei model), as this point concentrates the main contribution to $\Delta\tilde{\varepsilon}_{\omega}^{ib}$ in this spectral range [23]. The real part of $\Delta\tilde{\varepsilon}_{\omega}^{ib}(t)$ has been deduced from the imaginary part by a Kramers-Kronig analysis. Throughout the calculations, the electron distribution $f(E,t)$, where E stands for the electron energy, has been modeled via the Fermi-Dirac distribution law, assuming a thermalized distribution at each time step. Finally, the total transient differential dielectric function variation $[\Delta\tilde{\varepsilon}_{\omega}(t) = \Delta\tilde{\varepsilon}_{\omega}^{ib}(t) + \Delta\tilde{\varepsilon}_{\omega}^{D}(t)]$ has been added to the initial nonperturbed dielectric function of Au $(\tilde{\varepsilon}_{\omega}^{0})$ to determine the transient dielectric function at each delay time $[\tilde{\varepsilon}_{\omega}(t)]$. As the NPs are spread randomly on the SiO$_2$ NWs and present a random orientation relative to the incident field polarization direction, the Maxwell-Garnett effective medium approach extended for oblate-shaped NPs has been used to estimate the effective dielectric function $[\tilde{\varepsilon}_{\omega}^{\rm eff}(t)]$ at each time delay [24,25]. To this end, a fictitious homogeneous host medium embedding the NPs has been considered, the dielectric function of which $(\varepsilon^{\rm hm})$ is evaluated as the surface-area-weighted average value of those of air $(\varepsilon^{\rm air})$ and SiO$_2$ $(\varepsilon^{\rm silica})$:

$$\varepsilon^{\rm hm} = q\varepsilon^{\rm silica} + (1-q)\varepsilon^{\rm air}, \qquad (5)$$

where q is the fraction of the NP surface in contact with the NW; from the observation of SEM images and NP shape, its value is estimated to be $q \approx 1/3$.

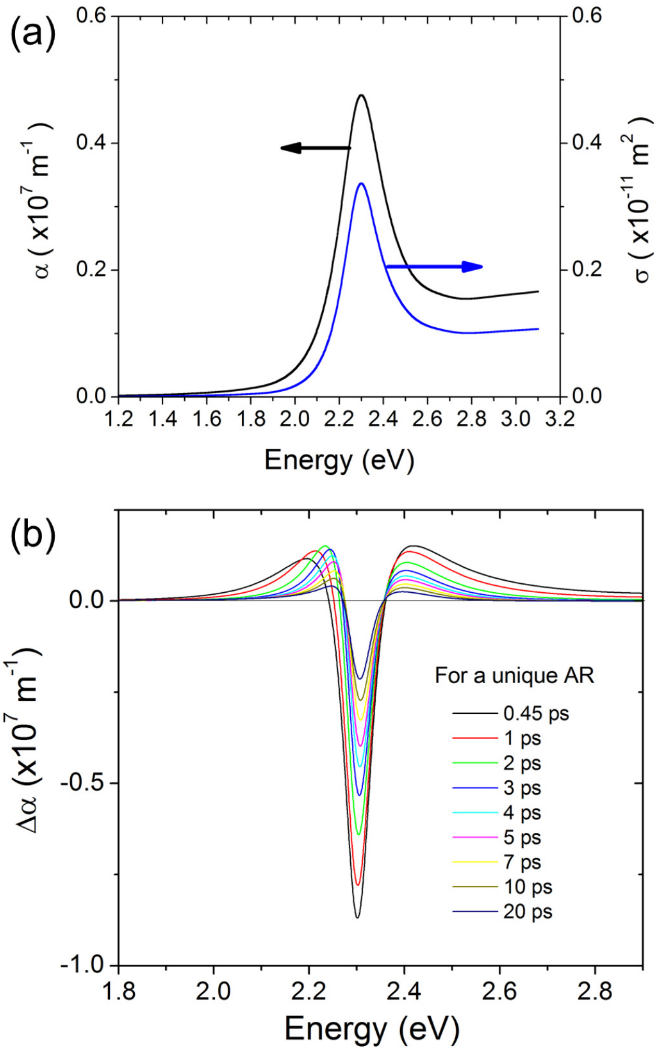

FIG. 4. (a) Calculated stationary optical properties: the left y axis (black) shows the absorption coefficient of the effective medium (randomly oriented oblate Au NPs with AR = 2.25 in the air-silica mixture) and the right y axis (blue) shows the absorption cross-section of an oblate Au NP with AR = 2.25. (b) Calculated spectral dependence of the pump-induced variation of the absorption coefficient $(\Delta\alpha)$ at different delay times for oblate Au NPs of AR = 2.25.

Similarly, as the heat generated in the NPs by electron-phonon collisions is released to the host medium through the contact interface, the corresponding surface weighted average of the thermal conductivity and the heat capacity of the fictitious medium, involved in the 3TM equations, are evaluated in the same way, where the individual thermal properties of silica and air are taken from Refs. [26] and [27], respectively.

Both stationary and transient optical responses of the arrays have been simulated. Based on the SEM images that indicate that the NPs have an ellipsoid shape, rather than a spherical one, we have used oblate ellipsoids to describe the NPs. Using an aspect ratio (AR) of 2.25, the simulated stationary LSPR matches that determined experimentally (2.3 eV), as shown in Fig. 4(a). In Fig. 4(a), the right y axis shows the stationary optical absorption cross-section spectrum as calculated using the Gans-Mie theory [28]. For comparison, the stationary effective absorption coefficient of the whole medium (Au NPs in the air-silica mixture) has also been calculated (left y axis) for a volume filling fraction $p = 0.02$. This value is chosen somehow arbitrarily as in the following the absolute magnitude of the absorption coefficient and its transient variation will not be compared directly with experimental data. It is chosen to be sufficiently small to avoid any significant mean-field effect in the width and location of the plasmon band. In both cases, the stationary dielectric function of Au ($\tilde{\varepsilon}^0_\omega$) has been taken from the experimental data reported by Palik [29]. The calculation is performed by integrating over all the possible NP orientations relative to the fixed field polarization direction in order to match the actual sample morphology [see Fig. 1(b)]. Hence two absorption bands are expected to appear in the spectra, corresponding to the two LSPR modes (polarization parallel or perpendicular to the oblate NP). However, for the chosen AR = 2.25 (and also for the other ARs that will be considered later), the two individual resonance peaks are not decoupled enough. Moreover, the oscillation strength associated with the field polarization along the short axis is very small and it results only in the broadening of the effective resonance peak, which mainly stems from the twofold degenerate in-plane resonance mode. This explains why the stationary absorption spectrum [Fig. 4(a)] exhibits a single LSPR band peaking at 2.3 eV, just as in the experimental stationary data.

The transient optical response has been calculated solving the 3TM equations. The absorption cross-section value, which was used to determine the instantaneous absorbed power, has been obtained by using the Gans-Mie theory at 405 nm (experimental pump wavelength). Figure 4(b) shows the calculated transient optical absorption of a Au NP with AR = 2.25. First of all, it should be noted that the use of the 3TM at short times ($t < 1$ ps) is only a rather approximate approach as the athermal regime for the electron gas cannot be accurately described by a pure thermal model [19,21]. Nonetheless, the computed spectral signature and its evolution with time depicted in Fig. 4(b) have strong similarities with the experimental results.

However, some differences can be seen in both stationary and transient spectra: (i) the theoretical profiles are narrower than the experimental ones, (ii) the spectral location of the bleaching of the LSPR in the calculated data remains almost constant (with a minimum at about 2.3 eV) over the whole time range under investigation, and (iii) the balance of the right and left positive wings of the theoretical curve is more asymmetric. Furthermore, the very small blue shift observed for single ARs is much smaller than the experimental one of about 50 meV, always being less than 5 meV (hardly visible in Fig. 4). We emphasize the fact that the actual sample presents a quite broad dispersion in NP shape, as shown by the SEM image [Fig. 1(b)]. As the LSPR mode energy depends on this shape, we have investigated the influence of a nonuniform NP shape distribution on the stationary and transient optical response. With this aim in mind, we have considered four additional oblate Au nanospheroids with equally spaced ARs, around the central value of 2.25 (1.75, 2.00, 2.25, 2.50, and 2.75) [see Fig. 5(a)], following the method reported in Ref. [21]. It should be noted that the goal was not to try to reproduce exactly the experimental findings by accounting for the actual shape distribution of the array, but rather to demonstrate qualitatively the effects of a shape distribution on the characteristics of the optical response. Figure 5(b) shows the stationary optical absorption spectra obtained for the five different ARs taken into account and their average value. Lower energies for the LSPR maximum correspond to higher ARs, as expected considering the increase of the length of the longer axis of the NP [30]. The LSPR signal of the average spectrum is centered around 2.3 eV, in agreement with the experimental spectrum, and it has a broader linewidth compared to the spectra obtained for individual ARs. Figure 5(c) shows the spectral dependence of the differential absorption coefficient for the five different ARs and their average value, at 4 ps delay time after the pump pulse maximum. The spectra show that the asymmetry of the two positive wings can be modified when accounting for the shape distribution. In addition, the spectral profile of the average is broadened and damped by the effect of the shape distribution, just as observed in the stationary

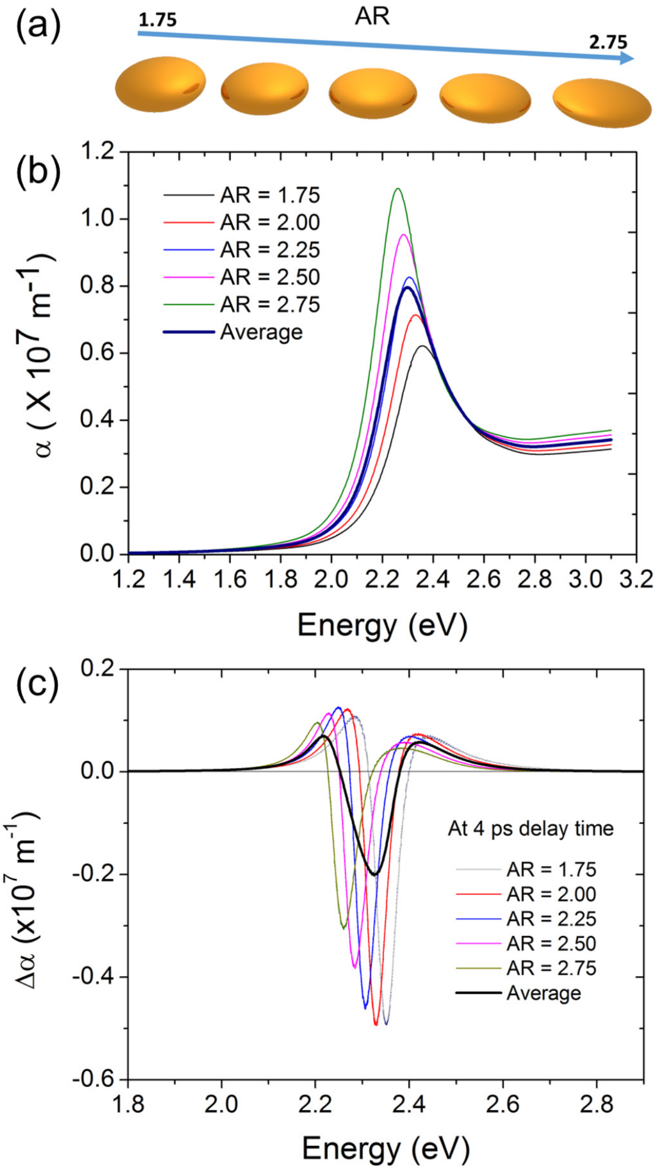

FIG. 5. (a) Graphic representation of the five ARs (1.75, 2.00, 2.25, 2.50, and 2.75) considered for the oblate Au NPs. (b) Calculated spectra of the absorption coefficient for NPs with different ARs and their average value. (c) Calculated spectral dependence of $\Delta\alpha$ for NPs with different ARs and their average value at 4 ps delay.

absorbance. The shape-averaged calculated spectrum is closer to the experimental spectrum than that calculated for a single AR in terms of both the balance between the two positive wings and the width of the spectral profile.

The variation of the shape-averaged spectrum with the delay time is reported in Fig. 6(a). The shape-averaged spectra can reproduce the shift of the minimum observed experimentally. A zoom into the minima of the spectra [Fig. 6(b)] clearly shows the blue shift of the minimum as the delay time increases, which was almost not observed when considering a single AR. A closer look at the two positive wings [Fig. 6(c)] demonstrates that the model better reproduces the experimental time evolution when the shape average of different ARs is introduced.

V. DISCUSSION

Examination of the stationary optical response of the array [Fig. 2(a)], reveals that the position and linewidth of the LSPR can be correlated with the size and shape of the NPs. It should be noted that a given relative variation of the NP shape has a larger effect on the LSPR position than a similar relative variation of the NP size [30]. The calculations performed [Figs. 4(a) and 5(b)] show that the LSPR position can be accurately reproduced considering Au NPs with the shape of oblate ellipsoids and an AR of 2.25. The broader linewidth of experimental spectra can be explained by taking into account a distribution of the AR value around the mean value of 2.25. It is worth noting that the environment around the NPs can also affect the linewidth but its effect is reported to be significant only for NPs larger than 100 nm [31], a size well above that of the Au NPs of our arrays.

Moving to the ultrafast transient optical response [Fig. 2(b)], the experimental spectral profiles are consistent with those reported in the literature for other Au NP systems [32,33]. Thanks to our simulations [Figs. 4(b), 5(c), and 6] that better account for the real morphology of our 3D NP array than a model considering only a single NP shape, we have been able to assign several characteristics observed in the experimental transient optical response to the effect of the distribution of the NP shape. In particular, the profile of the two positive wings is strongly related to the shape and to the shape distribution of the NPs, as expected from the observation of quite different behaviors in spherical and rodlike NPs [21,32,34].

The spectra shown in Fig. 6 are the result of the different optical dynamics of NPs with different ARs. In particular, the absorption bleaching relaxes more rapidly for larger ARs as can be seen in Fig. 7. As a result of the simulation, the shape averaging is able to qualitatively reproduce the observed blue shift of the negative minimum with increasing time.

The theoretical analysis of the temporal response of different ARs shows that carriers and lattice temperatures vary with different characteristic times for different ARs, as shown in Figs. 8(a) and 8(b), respectively. The curves are calculated by accounting for the different values of the absorption cross section at the pump laser wavelength for the different ARs, then resulting in a higher power absorbed for larger ARs. Figure 8(a) shows that the electron temperature relaxation

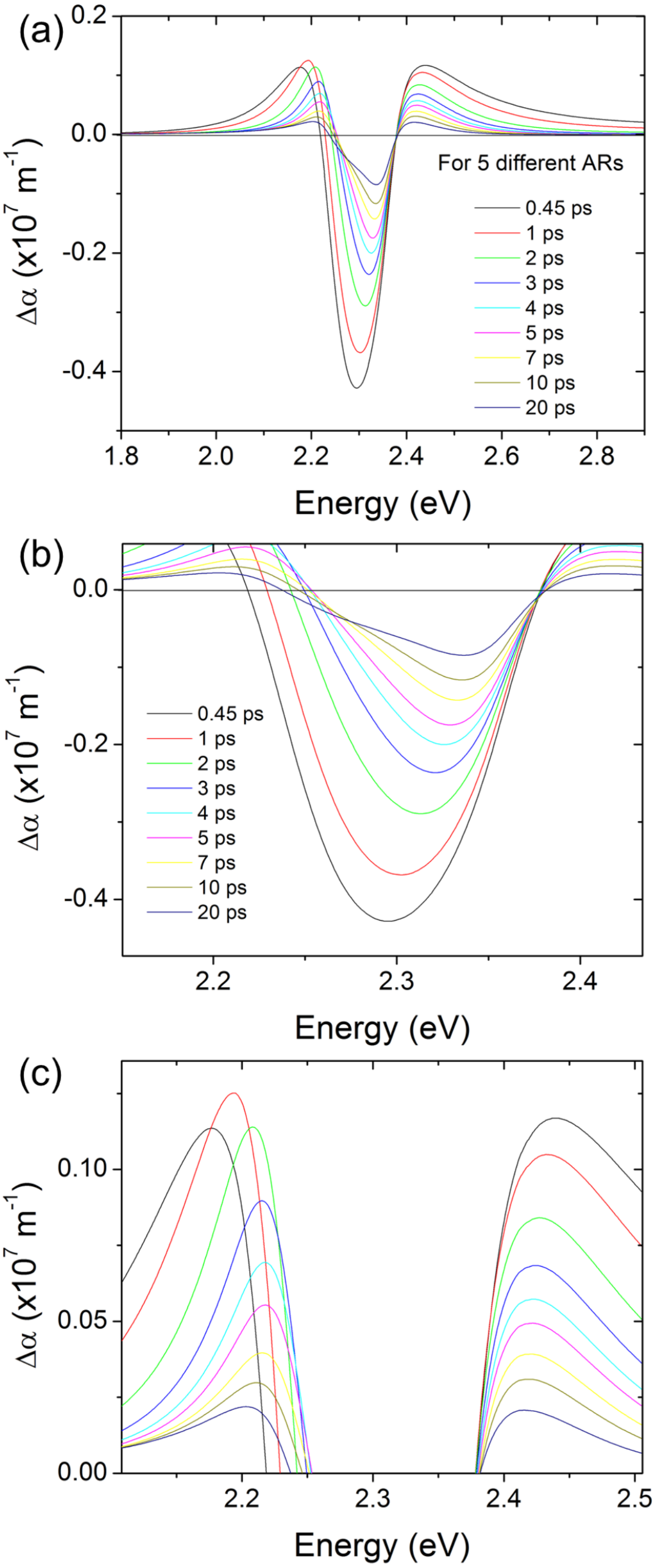

FIG. 6. (a) Spectra at different delay times, calculated as the average value over five arbitrary ARs. (b) Close-up of the minimum, which clearly shows the blueshift with increasing delay time. (c) Close-up of the two positive wings, which shows the time evolution of the symmetry between the two peaks.

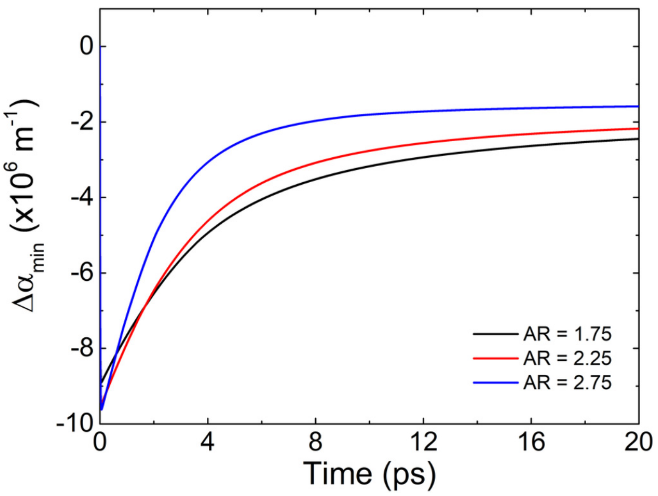

FIG. 7. Time evolution of the negative minimum of the absorption modification corresponding to the plasmon bleaching, as calculated for three NPs with AR = 1.75 (black), 2.25 (red), and 2.75 (blue), respectively.

time is slightly longer for larger ARs, a feature that, however, cannot explain the observed blueshift of the minimum negative absorption variation for increasing delay time. The different absorbed energy for varying AR could account for the different relaxation times of T_e displayed in Fig. 8(a), as it affects the initial maximum electron temperature reached and, as a result, the electron gas heat capacity. However, additional calculations (not shown) performed for different ARs but with the same absorbed energy exhibit the same behaviors. The proper interpretation lies rather in the dynamics of the lattice temperature: due to lower surface-to-volume ratio, larger AR NPs exhibit a slower heat release to the surrounding medium through the interface [Eq. (3)]; T_l then reaches higher values for higher ARs, as shown in Fig. 8(b), which slows down the relaxation dynamics of T_e. The effect of the different C_e values when accounting for the different pump energy absorbed just reinforces the trend within the first picoseconds after excitation, during which T_e is still significantly higher than T_l.

We further observe that, while the dynamics of T_e and T_l of course do not depend on the probe photon energy, the dynamics of the transient absorption does. Although there exists a link between the relaxation dynamics of the temperatures and the dynamics of the optical signal, this link is not straightforward. The complex dynamics of the electron distribution, the electron scattering rate and the transition probabilities for the different photon energies have to be considered to interpret the transient signal [35]. Then, we cannot base the interpretation of the dynamics of the optical signal solely on the knowledge of the dynamics of the electron temperature.

In order to better understand the origin of the AR-dependent relaxation time, we have extracted from the calculated dynamics an effective characteristic relaxation time, even if for some photon energies close to the plasmon mode this is somehow arbitrary as the sign of the transient absorption changes along time. The results are displayed in Fig. 9. First, one can notice that at low (<2.2 eV) and high (>2.8 eV) photon energies the relaxation times for the two ARs are rather close to each other, especially in the red part of the spectrum. Nevertheless, for AR = 1.75, the relaxation time is slightly higher than for AR = 2.75. This small homogeneous discrepancy can be ascribed to the dynamics of the intraband transition (Drude) contribution to the dielectric function. Indeed, the dominant term in the conduction electron scattering rate involved in this contribution is the one stemming from electron-phonon collisions, which is proportional to the metal lattice temperature [35]. As the dynamics of T_l is faster for high AR than for low AR [see the slopes of the curves in Fig. 8(b)], the dynamics of the Drude contribution is also faster, which explains the small, almost spectrally independent, discrepancy background, between the two curves of Fig. 9. In contrast, a large difference in relaxation times is superimposed on this background in the range from ∼2.2 to ∼ 2.8 eV. This interval, which is close to the interband transition threshold associated with the L point of the Brillouin zone, is the energy range considered in the model (the transitions close to the X point, starting from 1.8 eV, almost do not contribute to the transient signal [22]). The vertical dashed lines on Fig. 9 denote the position of the LSPR, which roughly corresponds to the negative minimum in the transient differential absorption. In this region, the relaxation

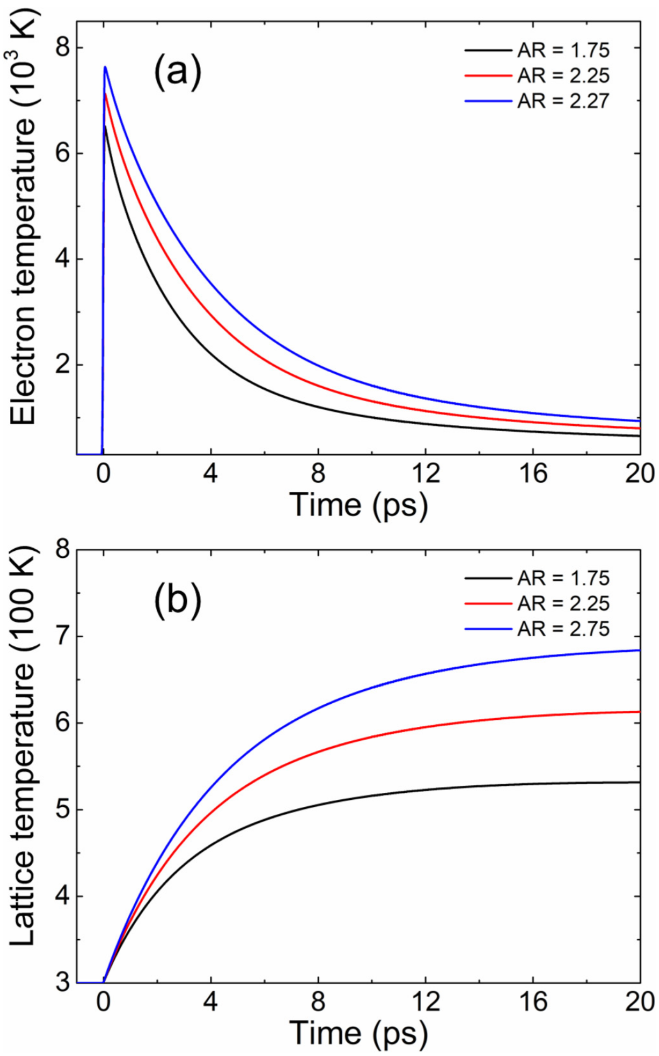

FIG. 8. Time evolution of the electron (a) and metal lattice (b) temperatures, as calculated by the 3TM for three NPs with AR = 1.75 (black), 2.25 (red), and 2.75 (blue), respectively.

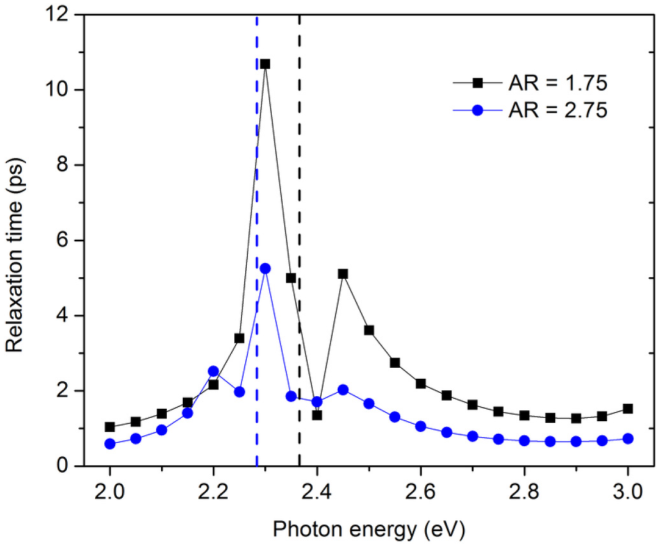

FIG. 9. Effective relaxation time of the transient optical signal as a function of probe photon energy, as extracted from the dynamics calculated for two NPs with AR = 1.75 (black) and 2.75 (blue), respectively. The dashed vertical lines denote the spectral location of the corresponding LSPR mode.

time for AR = 1.75 is significantly larger than for AR = 2.75. Beyond ∼2.45 eV, the gap decreases progressively with increasing photon energy towards the blue end of the LSPR, beyond which only the small and almost spectrally independent contribution mentioned above remains. This difference can be only attributed to the coupling of the LSPR with interband transitions: as the LSPR for low ARs lies at higher photon energy than for large ARs, this coupling is stronger and results in slower dynamics. This explains the amplified blueshift when mixing different ARs, corroborating what was shown in Fig. 7.

We can then conclude that the blueshift observed when accounting for the shape distribution can be ascribed to the slowing down of the relaxation, in the vicinity of the LSPR, with decreasing AR. This trend cannot be simply interpreted in terms of temperature dynamics, but rather by invoking the stronger coupling of the plasmon resonance with interband transitions.

Finally, in Fig. 10, we show the position of both the experimental and theoretical minima as a function of the delay time. Experimentally, the minimum reaches the energy value of 2.33 eV in about 20 ps and then remains at a constant energy. The shift depends on the pump pulse intensity: at higher intensities we observe stronger shifts of the minimum position and longer times are needed to reach the final value. Small differences (∼10 meV) have been observed in the final value of the minimum energy, depending on the pump power. As mentioned above, the quantitative behaviors depend on the real shape distribution that is certainly different from the one used in the model. The steeper profile of the calculated blue shift hence reflects the semiarbitrary choice of the shape distribution in the model. We point out once more, however, that the simulations clearly indicate that the blue shift stems from the presence of a shape distribution in the Au NP array. The higher position of the theoretical points indicates that the real NP shape distribution, partly dictated by the NW shape, is weighted towards higher ARs than that the arbitrary one used in the simulation.

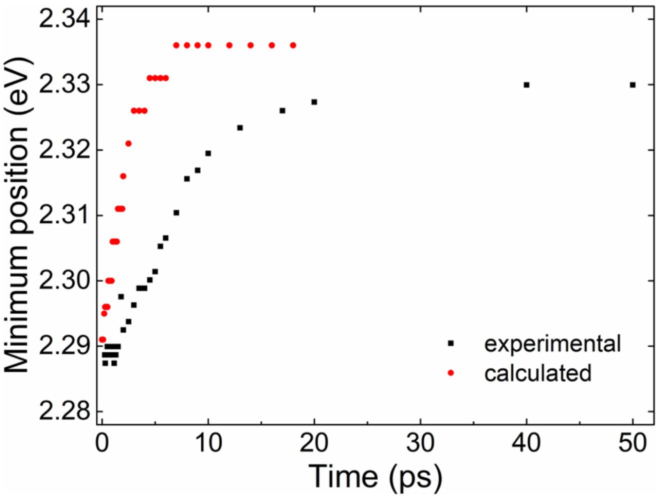

FIG. 10. Position of the main minimum in the ΔA measurements (black squares) and in the $\Delta\alpha$ calculation (red dots) as a function of the delay time between pump and probe pulses.

As a last remark, we notice that the measured e-ph scattering time constant of 0.95 ps [see Fig. 3(b)] agrees with that expected considering the NP size [16]. Indeed, the electron-phonon coupling constant is affected by the NP size only for sizes below 5 nm, while the NP shape has no effect on this time constant [17].

VI. CONCLUSION

In conclusion, Au-decorated SiO_2 NW arrays have been fabricated on quartz substrates, starting from Si NWs. The optical properties of the Au NPs on top of the array have been investigated in both the stationary and dynamic regimes by means of absorption and transient absorption spectroscopies, respectively. By developing a two-step, three-temperature model we have been able to reproduce the stationary spectrum as well as the qualitative spectral dependence of the transient absorption profile obtained from the experiment. Indeed, using an arbitrary set of Au NPs with different aspect ratios, we have demonstrated that the width of the experimental spectra, the blueshift of the absorption bleaching along the relaxation and the asymmetry between the two positive wings of the absorption variation spectrum can all be attributed to the nonuniform shape distribution of the Au NPs in the sample. We have observed that the temporal behavior of the carrier and lattice temperatures alone is not sufficient to explain the experimental features and in particular the blue shift. The latter can be interpreted by invoking the stronger coupling of the plasmon resonance with interband transitions in nanoparticles with smaller aspect ratio. This has an AR-dependent effect on the carrier relaxation dynamics that gives rise to the observed blueshift with increasing delay time.

The stationary and dynamic features observed in the plasmon resonance of our system suggest that in presence of a shape distribution of metal nanoparticles, the effects relying on their properties should be properly weighed. This is an important point to be kept in mind when designing sensors or catalysts based on a dewetting technique that, in turn, is a much easier and quicker technology if compared to the use of monodispersed, separately prepared nanoparticles. In particular for catalysts, where hot electrons play a crucial role [36], the different contributions to carrier cooling due to different shapes must be taken into account, as pointed out in the present work. Finally, we notice that the use of nanowires as substrates, where the nanoparticle coarsening occurs, introduces constraints on the atom diffusion on the NW sidewalls that influences the final result in terms of shape and size. Tuning the metal film thickness, the annealing temperature and duration, metal NPs with variable shape can be obtained with designed plasmon relaxation characteristics.

[1] K. A. Willets and R. P. Van Duyne, Annu. Rev. Phys. Chem. **58**, 267 (2007).

[2] X. Huang, I. H. El-Sayed, W. Qian, and M. A. El-Sayed, J. Am. Chem. Soc. **128**, 2115 (2006).

[3] S. A. Maier, M. L. Brongersma, P. G. Kik, S. Meltzer, A. A. G. Requicha, and H. A. Atwater, Adv. Mater. **13**, 1501 (2001).

[4] C. L. Haynes and R. P. Van Duyne, J. Phys. Chem. B **105**, 5599 (2001).

[5] C. J. Murphy, T. K. San, A. M. Gole, C. J. Orendorff, J. X. Gao, L. Gou, S. E. Hunyadi, and T. Li, J. Phys. Chem. B **109**, 13857 (2005).

[6] G. V. Hartland, Chem. Rev. **111**, 3858 (2011).

[7] S. Enoch, R. Quidant, and G. Badenes, Opt. Express **12**, 3422 (2004).

[8] J. Ye, K. Bonroy, D. Nelis, F. Frederix, J. D'Haen, G. Maes, and G. Borghs, Colloids Surf. A **321**, 313 (2008).

[9] E. Galopin, J. Barbillant, Y. Coffinier, S. Szunerits, G. Patriarche, and R. Boukherroub, ACS Appl. Mater. Interfaces **1**, 1396 (2009).

[10] D. Naumenko, V. Zannier, V. Grillo, D. Cassese, G. Priante, S. Dal Zilio, S. Rubini, and M. Lazzarino, Nanoscale **6**, 13651 (2014).

[11] A. Convertino, M. Cuscunà, F. Martelli, M. G. Manera, and R. Rella, J. Phys. Chem. C **118**, 685 (2014).

[12] W. H. Hung, M. Aykol, D. Valley, W. Hou, and S. B. Cronin, Nano Lett. **10**, 1314 (2010).

[13] S. Navalon, M. de Miguel, R. Martin, M. Alvaro, and H. Garcia, J. Am. Chem. Soc. **133**, 2218 (2011).

[14] A. Convertino, M. Cuscunà, and F. Martelli, Nanotechnology **21**, 355701 (2010).

[15] G. V. Hartland, Annu. Rev. Phys. Chem. **57**, 403 (2006).

[16] J. H. Hodak, I. Martini, and G. V. Hartland, Chem. Phys. Lett. **284**, 135 (1998).

[17] A. Arbouet, C. Voisin, D. Christofilos, P. Langot, N. Del Fatti, F. Vallee, J. Lerme, G. Celep, E. Cottancin, M. Gaudry, M. Pellarin, M. Broyer, M. Maillard, M. P. Pileni, and M. Treguer, Phys. Rev. Lett. **90**, 177401 (2003).

[18] M. Rashidi-Huyeh and B. Palpant, J. Appl. Phys. **96**, 8 (2004).

[19] T. Labouret and B. Palpant, Phys. Rev. B **94**, 245426 (2016).

[20] Z. Lin, L. V. Zhigilei, and V. Celli, Phys. Rev. B **77**, 075133 (2008).

[21] Y. Guillet, M. Rashidi-Huyeh, and B. Palpant, Phys. Rev. B **79**, 045410 (2009).

[22] X. Wang, Y. Guillet, P. R. Selvakannan, H. Remita, and B. Palpant, J. Phys. Chem. C **119**, 7416 (2015).

[23] M. Guerrisi, R. Rosei, and P. Winsemius, Phys. Rev. B **12**, 557 (1975).

[24] S. Norrman, T. Andersson, C. G. Granqvist, and O. Hunderi, Phys. Rev. B **18**, 674 (1978).

[25] V. A. Fedotov, V. I. Emel'yanov, K. F. MacDonald, and N. I. Zheludev, J. Opt. A-Pure Appl. Opt. **6**, 155 (2003).

[26] N. P. Bansal and R. H. Doremus, *Handbook of Glass Properties* (Academic Press, London, 1986).

[27] R. A. Guereca, H. P. Richardson, J. L. Gordon, J. D. Walker, and J. L. Cooper, *Thermophysical Properties of Selected Gases Below 300 °K* (U.S. Bur. Mines Inf. Circ. 8317, 1967).

[28] R. Gans, Ann. Phys. **47**, 270 (1915).

[29] E. D. Palik, *Handbook of Optical Constants of Solids* (Academic Press, 1998), Vol. 3.

[30] S. Link, M. B. Mohamed, and M. A. El-Sayed, J. Phys. Chem. B **103**, 3073 (1999).

[31] A. Wokaun, J. P. Gordon, and P. F. Liao, Phys. Rev. Lett. **48**, 957 (1982).

[32] Y. Guillet, E. Charron, and B. Palpant, Phys. Rev. B **79**, 195432 (2009).

[33] M. Perner, P. Bost, U. Lemmer, G. von Plessen, J. Feldmann, U. Becker, M. Mennig, M. Schmitt, and H. Schmidt, Phys. Rev. Lett. **78**, 2192 (1997).

[34] H. Baida, D. Mongin, D. Christofilos, G. Bachelier, A. Crut, P. Maioli, N. Del Fatti, and F. Vallée, Phys. Rev. Lett. **107**, 057402 (2011).

[35] X. Wang, Ph.D. thesis, University Pierre et Marie Curie, Paris, 2013.

[36] S. Mukherjee, F. Libisch, N. Large, O. Neumann, L. V. Brown, J. Cheng, J. Britt Lassiter, E. A. Carter, P. Nordlander, and N. J. Halas, Nano Lett. **13**, 240 (2013).